

Further Real Data Experimental Results for “An Outlier-insensitive Unmixing Algorithm with Spatially Varying Hyperspectral Signatures”

Technical Report

Yao-Rong Syu[†], Chia-Hsiang Lin^{*}, and Chong-Yung Chi[†]

January 28, 2019

[†]Institute of Communications Engineering, National Tsing-Hua University, Hsinchu, Taiwan 30013, R.O.C.

^{*} Center for Space and Remote Sensing Research, National Central University, Taoyuan, Taiwan 32001, R.O.C.

E-mail: roy50408@gmail.com, chiahxiang.steven.lin@gmail.com, cychi@ee.nthu.edu.tw

1 ABSTRACT

This technical report provides further experimental results for the paper “An Outlier-insensitive Algorithm for Unmixing Spatially Varying Hyperspectral Images” [1], in which a new hyperspectral unmixing (HU) algorithm, called the variability/outlier-insensitive multiconvex (VOIMU) algorithm, is proposed for tackling both endmember variability (EV) and outlier effects (OE) present in the given data set at the same time. The efficacy of the proposed VOIMU algorithm has been demonstrated using two real datasets for which the number of endmembers is $N = 3$ and the data size $L = 50 \times 50$ and $L = 50 \times 90$ [1]. In this report, we provide more experimental results with $N = 9$ [2,3] and a larger data size $L = 150 \times 150$ to further support the effectiveness and practical applicability of this algorithm.

2 INTRODUCTION

For ease of the ensuing presentation, some notations are defined collectively hereinafter.

- N , M , and L denote the total numbers of endmembers, spectral bands, and pixels, respectively;
- $\mathcal{I}_L \triangleq \{1, \dots, L\}$ for any positive integer L ;
- $\{\mathbf{A}_n\}$ represents the set of \mathbf{A}_n for all the admissible values of n ;
- \succeq stands for the componentwise inequality;
- $\mathbf{0}_{M \times N}$ denotes the all-zero $M \times N$ matrix;
- $\mathbf{1}_M$ denotes all-one M -vector.

The VOIMU algorithm is designed for solving the following nonconvex problem:

$$\begin{aligned}
& \min_{\{\mathbf{A}_n\}, \bar{\mathbf{A}}, \mathbf{S}} \frac{1}{2} \sum_{n=1}^L [\|\mathbf{x}_n - \mathbf{A}_n \mathbf{s}_n\|_2^2 + \epsilon]^{p/2} \\
& \quad + \lambda_1 \sum_{n=1}^L \phi_1(\mathbf{A}_n, \bar{\mathbf{A}}) + \lambda_2 \phi_2(\bar{\mathbf{A}}) \\
\text{s.t. } & \mathbf{S} \succeq \mathbf{0}_{N \times L}, \mathbf{S}^T \mathbf{1}_N = \mathbf{1}_L, \\
& \mathbf{A}_n \succeq \mathbf{0}_{M \times N}, \forall n \in \mathcal{I}_L,
\end{aligned} \tag{1}$$

where

- $\lambda_1, \lambda_2 > 0$ are regularization parameters;
- ϵ is a small positive real number;
- $0 < p < 1$;
- $\mathbf{x}_n \in \mathbb{R}^M$ is the given hyperspectral data;
- $\mathbf{A}_n \triangleq [\mathbf{a}_{1,n}, \dots, \mathbf{a}_{N,n}] \in \mathbb{R}^{M \times N}$ is the endmember spectral signature matrix;
- $\mathbf{S} \triangleq [\mathbf{s}_1, \dots, \mathbf{s}_L]$, where $\mathbf{s}_n \in \mathbb{R}^N$ is the abundance vector of pixel n ;
- $\bar{\mathbf{A}} \triangleq [\bar{\mathbf{a}}_1, \dots, \bar{\mathbf{a}}_N] \in \mathbb{R}^{M \times N}$ (a reference endmember signature matrix);
- $\phi_1(\mathbf{A}_n, \bar{\mathbf{A}}) \triangleq \frac{1}{2} \|\mathbf{A}_n - \bar{\mathbf{A}}\|_F^2$;
- $\phi_2(\bar{\mathbf{A}}) \triangleq \frac{1}{2} \sum_{i=1}^{N-1} \sum_{j=i+1}^N \|\bar{\mathbf{a}}_i - \bar{\mathbf{a}}_j\|_2^2$.

The VOIMU algorithm is implemented by an alternating algorithm, referred to as Algorithm 1 in [1], for solving (1). Given λ_1, λ_2, p , and ϵ , Algorithm 1 yields a stationary point, denoted as $\{\mathbf{z}^*, \{\mathbf{A}_n^*\}, \bar{\mathbf{A}}^*, \mathbf{S}^*\}$, of problem (1), where $\mathbf{z}^* = [z_1^*, \dots, z_L^*] \succeq \mathbf{0}_L$ is an auxiliary vector and the distribution of the normalized $1/z_n^*$ (cf. Figure 16) indicates potential outlier pixels (including pixel locations and relative magnitudes).

3 FURTHER EXPERIMENTAL RESULTS

We follow the same procedure for the real data experiment as in the main paper and use the corresponding performance measures for the performance evaluation:

- Spectral angle error (SAE) [3]:

$$\text{SAE} \triangleq \sqrt{\frac{1}{N} \sum_{m=1}^N \left[\arccos \frac{(\mathbf{a}_{m_{lib}})^T \bar{\mathbf{a}}_m}{\|\mathbf{a}_{m_{lib}}\|_2 \cdot \|\bar{\mathbf{a}}_m\|_2} \right]^2},$$

where $\mathbf{a}_{m_{lib}}$ is the library spectrum from USGS library of the m -th material, and $\bar{\mathbf{a}}_m$ is the associated reference endmember signature estimate.

- The spectral angle distance ϕ [3]:

$$\phi = \arccos \left(\frac{(\mathbf{a}_{m_{lib}})^T \bar{\mathbf{a}}_m}{\|\mathbf{a}_{m_{lib}}\|_2 \cdot \|\bar{\mathbf{a}}_m\|_2} \right).$$

- Reconstruction error (RE) [4]:

$$RE \triangleq \frac{1}{M(L-Z)} \sum_{n \in \mathcal{I}_L \setminus \mathcal{Z}} \|\mathbf{x}_n - \hat{\mathbf{x}}_n\|_2^2.$$

where $\hat{\mathbf{x}}_n = \hat{\mathbf{A}}_n \hat{\mathbf{s}}_n$ is the associated estimate in which $\hat{\mathbf{A}}_n$ is the endmember matrix estimate.

- Average reconstruction spectral angle mapper ($xSAM$) [5]:

$$xSAM \triangleq \frac{1}{L-Z} \sum_{n \in \mathcal{I}_L \setminus \mathcal{Z}} \arccos \left(\frac{(\mathbf{x}_n)^T \hat{\mathbf{x}}_n}{\|\mathbf{x}_n\|_2 \cdot \|\hat{\mathbf{x}}_n\|_2} \right),$$

A sub-image of size $L = 150 \times 150$ taken from the hyperspectral image of the well-known AVIRIS Cuprite dataset as shown in Figure 1, with low SNR bands removed, the left 183 exploitable spectral bands are used in the experiment (with the bands 5-106, 115-151, and 171-214). This sub-image has been extensively studied in HU literature, for which the number of endmembers is known as $N = 9$ [3]. The experiment is performed for two cases as follows:

- Case 1: No artificial outliers added to the original dataset;
- Case 2: 10 artificial outliers added to the original dataset.

The proposed VOIMU algorithm is employed to process the data for the above two cases. The same data are also used to test the SDVMM-RASF/FCLS algorithm [6, 7] that is only robust against OE, and PLMM [4] and ELMM [5] algorithms that can only handle EV, and vertex component analysis (VCA)/FCLS [7,8] that is a benchmark HU algorithm based on LMM without considering both EV and OE, just serving as a baseline for performance comparison. The parameters used for the proposed VOIMU algorithm are $p = 0.5$, $\lambda_1 = 0.5$, $\lambda_2 = 10$, $\epsilon = 10^{-3}$, $L_s = 25$, and stopping criterion is 2×10^{-3} (parameters in Algorithm 1). Those used for PLMM and ELMM are $(\alpha, \beta, \gamma) = (0, 10^2, 1)$ and $(\lambda_S, \lambda_A, \lambda_\psi) = (0.4, 5 \times 10^{-3}, 5 \times 10^{-3})$, respectively.

The experimental results in terms of RE, $xSAM$, SAE and running times for Case 1 and Case 2 are shown in Table 1 and Table 2, respectively. The estimated nine abundance maps are shown in Figures 2-6 and Figures 7-11 for Case 1 and Case 2, respectively. From Table 1, one can observe that the VOIMU algorithm significantly outperforms all the other algorithms, PLMM and ELMM perform much better than VCA/FCLS and SDVMM-RASF/FCLS, although the estimated abundance maps are also quite similar to each other (cf. Figure 2-6). From Table 2, one can observe that the VOIMU algorithm still significantly outperforms the other algorithms.

From Table 3, which lists the spectral angle distances ϕ between each reference endmember signature estimate and the corresponding counterpart in USGS library for Case 1, one can observe that the identified materials by the VOIMU algorithm are Muscovite, Kaolinite, Pyrope, Hematite, Montmorillonite, Alunite, Buddingtonite, Chalcedony, and Nontronite. By comparing Figure 2-6

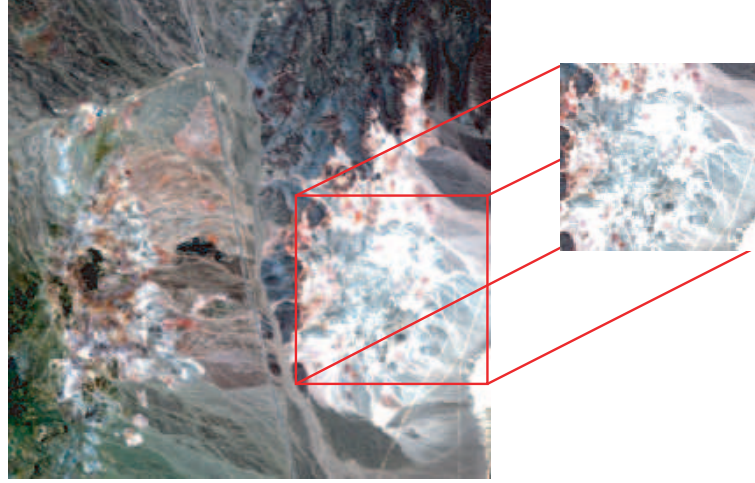


Figure 1. Sub-image of Cuprite mining site.

and Figure 7-11, we can see that the abundance maps associated with VOIMU and SDVMM-RASF/FCLS are much more reliable than those obtained by the other algorithms under test for Case 2, and OE has larger impact on the HU performance than EV.

Moreover, the square root EV energy distributions of VOIMU for Case 1 and Case 2 are shown in Figures 12 and 13, respectively, where the square root of EV energy associated with the m -th material in the n -th pixel is defined as

$$\frac{1}{\sqrt{M}} \|\mathbf{a}_{m,n} - \bar{\mathbf{a}}_m\|_2. \quad (2)$$

The nine estimated endmember signatures $\hat{\mathbf{A}}_n$ and the estimated reference signatures $\bar{\mathbf{A}}$ by VOIMU are shown in Figure 14 for Case 1, and Figure 15 for Case 2. Note that the results shown in Figures 14 and 15 are similar to each other for the two cases and so are those shown in Figure 14 and 15, demonstrating that VOIMU is robust against outliers. The distribution of the normalized $1/z_n^*$ in Case 1 is quite uniform, indicating no outliers in this dataset. The normalized $1/z_n^*$ exceeding a threshold (denoted by circles) for Case 2 in Figure 16 as well as the true artificial outliers (denoted as “*”), as shown in Figure 16 in addition to high coincidence between $1/z_n^*$ and the true artificial outliers (in both locations and relative magnitudes).

The above experimental results further support the efficacy and the applicability of the proposed VOIMU algorithm.

Table 1. Experimental results for Case 1 (without artificial outliers), where the boldface numbers denote the best performance.

Methods	Performance Measures			Running Time T (seconds)
	RE	x SAM	SAE	
VCA/FCLS	8.85e-05	1.81e-02	6.79e+00	8.83
SDVMM-RASF/FCLS	5.76e-05	1.69e-02	6.51e+00	7.04
PLMM	3.90e-06	4.73e-03	8.48e+00	1025.17
ELMM	9.79e-06	7.55e-03	6.80e+00	283.14
VOIMU	2.67e-08	3.45e-04	6.19e+00	865.97

Table 2. Experimental results for Case 2 (with 10 artificial outliers added), where the boldface numbers denote the best performance.

Methods	Performance Measures			Running Time T (seconds)
	RE	x SAM	SAE	
VCA/FCLS	7.37e-03	1.24e-01	2.06e+01	7.77
SDVMM-RASF/FCLS	5.76e-05	1.69e-02	6.51e+00	26.42
PLMM	1.05e-05	7.43e-03	1.86e+01	1809.77
ELMM	3.76e-05	1.29e-02	2.06e+01	509.76
VOIMU	2.67e-08	3.45e-04	6.19e+00	757.36

Table 3. Spectral angle distance between library spectra and endmember estimates for Case 1, where the boldface numbers correspond to the smallest values of ϕ .

	VOIMU	ELMM	PLMM	SDVMM-RASF	VCA
Muscovite	5.62	6.08	6.58	6.19	6.08
Kaolinite	6.31	-	-	7.02	-
Pyrope	4.12	5.29	4.91	3.81	5.31
Hematite	8.69	10.8	11.6	8.95	10.8
Montmorillonite	5.23	5.68	7.23	5.60	5.67
Alunite	8.77	6.77	5.96	8.41	6.72
Buddingtonite	4.14	6.45	8.38	4.31	6.45
Chalcedony	4.87	5.34	10.0	5.93	5.33
Nontronite	5.97	-	-	6.61	-
Andradite	-	4.11	4.67	-	4.08
Dumortierite	-	8.34	12.8	-	8.34
Average ϕ (degrees)	5.97	6.54	8.02	6.31	6.53
Time T (seconds)	866	283	1025	7.04	8.83

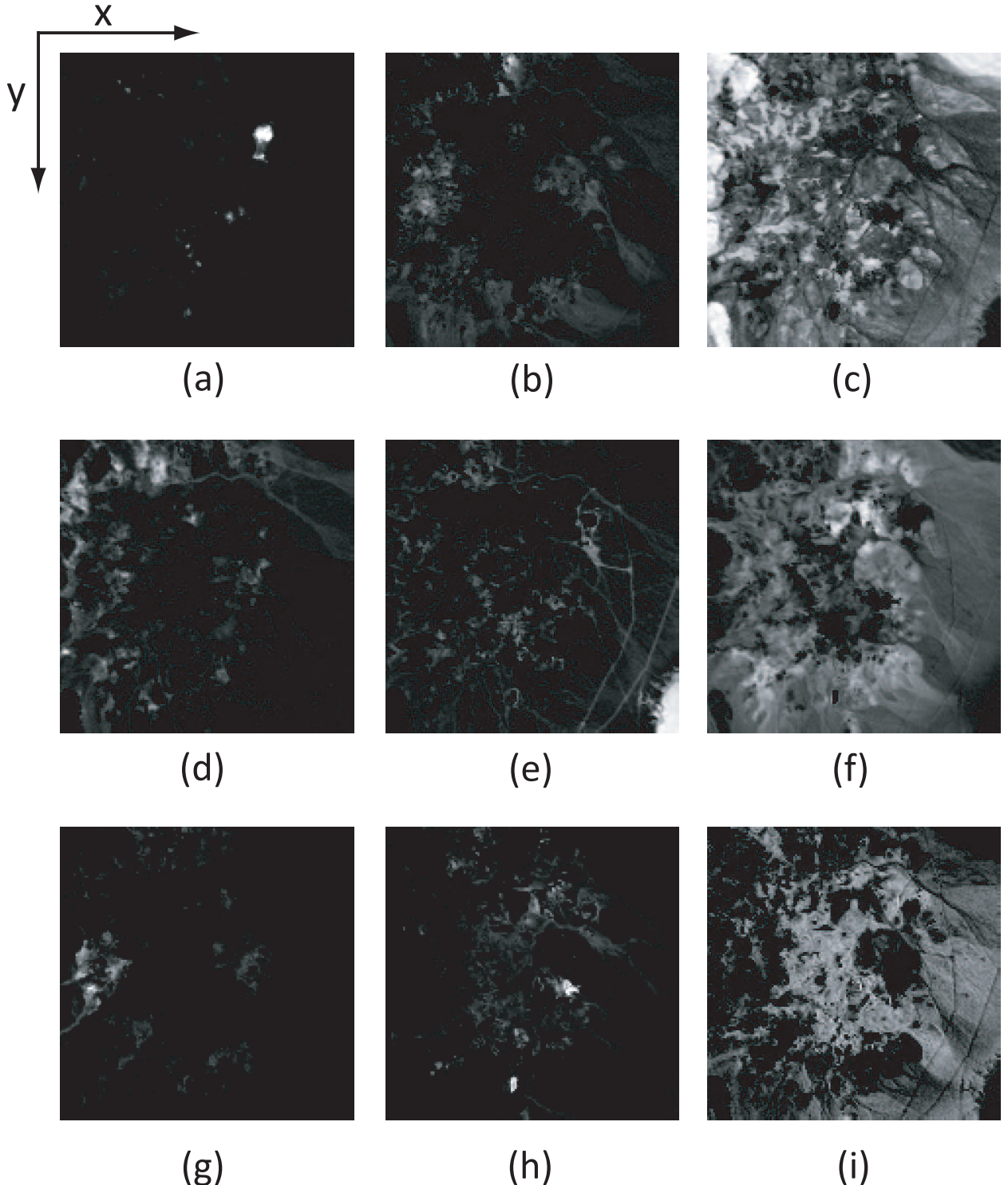


Figure 2. Nine estimated abundance maps by VCA/FCLS for Case 1 (without artificial outliers), where (a) Muscovite, (b) Dumortierite, (c) Pyrope, (d) Hematite, (e) Montmorillonite, (f) Alunite, (g) Buddingtonite, (h) Chalcedony, and (i) Andradite, and the gray level scale is between 0 (black) and 1 (white).

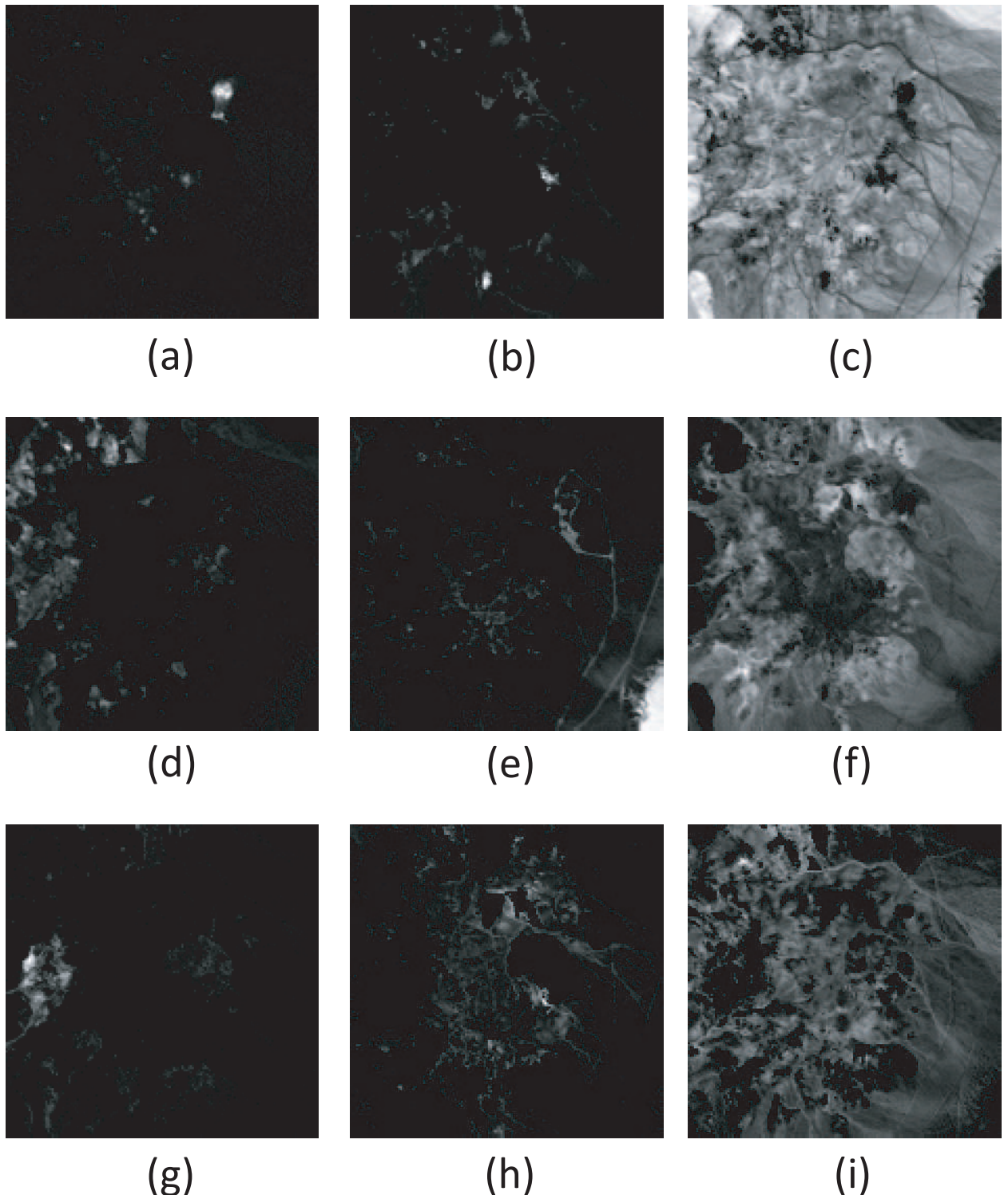
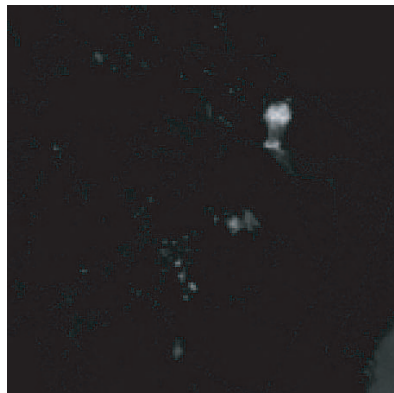


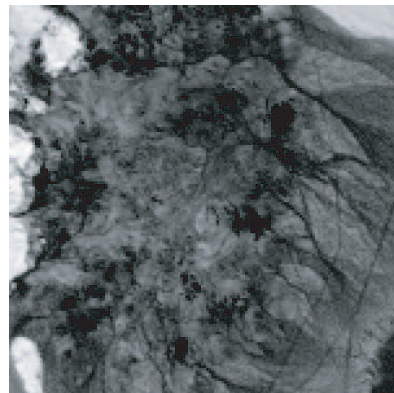
Figure 3. Nine estimated abundance maps by SDVMM-RASF/FCLS for Case 1 (without artificial outliers), where (a) Muscovite, (b) Kaolinite, (c) Pyrope, (d) Hematite, (e) Montmorillonite, (f) Alunite, (g) Buddingtonite, (h) Chalcedony, and (i) Nontronite, and the gray level scale is between 0 (black) and 1 (white).



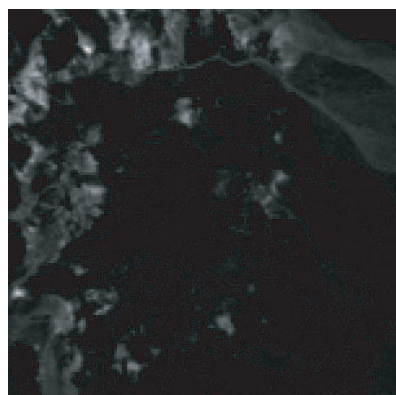
(a)



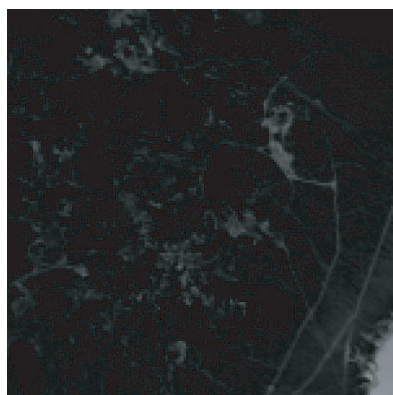
(b)



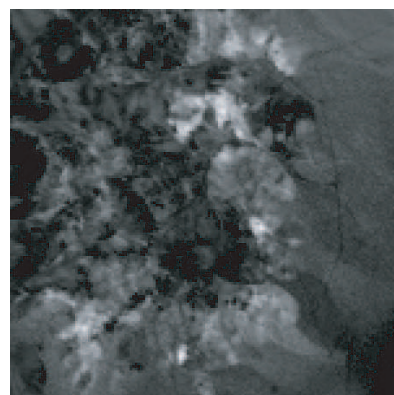
(c)



(d)



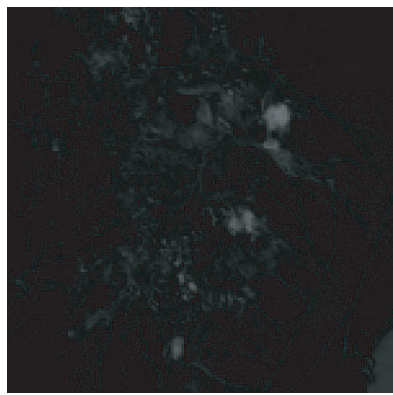
(e)



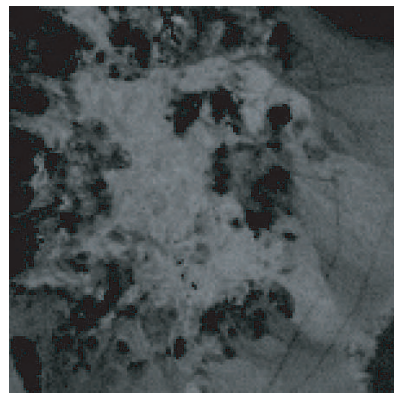
(f)



(g)



(h)



(i)

Figure 4. Nine estimated abundance maps by PLMM for Case 1 (without artificial outliers), where (a) Muscovite, (b) Dumortierite, (c) Pyrope, (d) Hematite, (e) Montmorillonite, (f) Alunite, (g) Buddingtonite, (h) Chalcedony, and (i) Andradite, and the gray level scale is between 0 (black) and 1 (white).

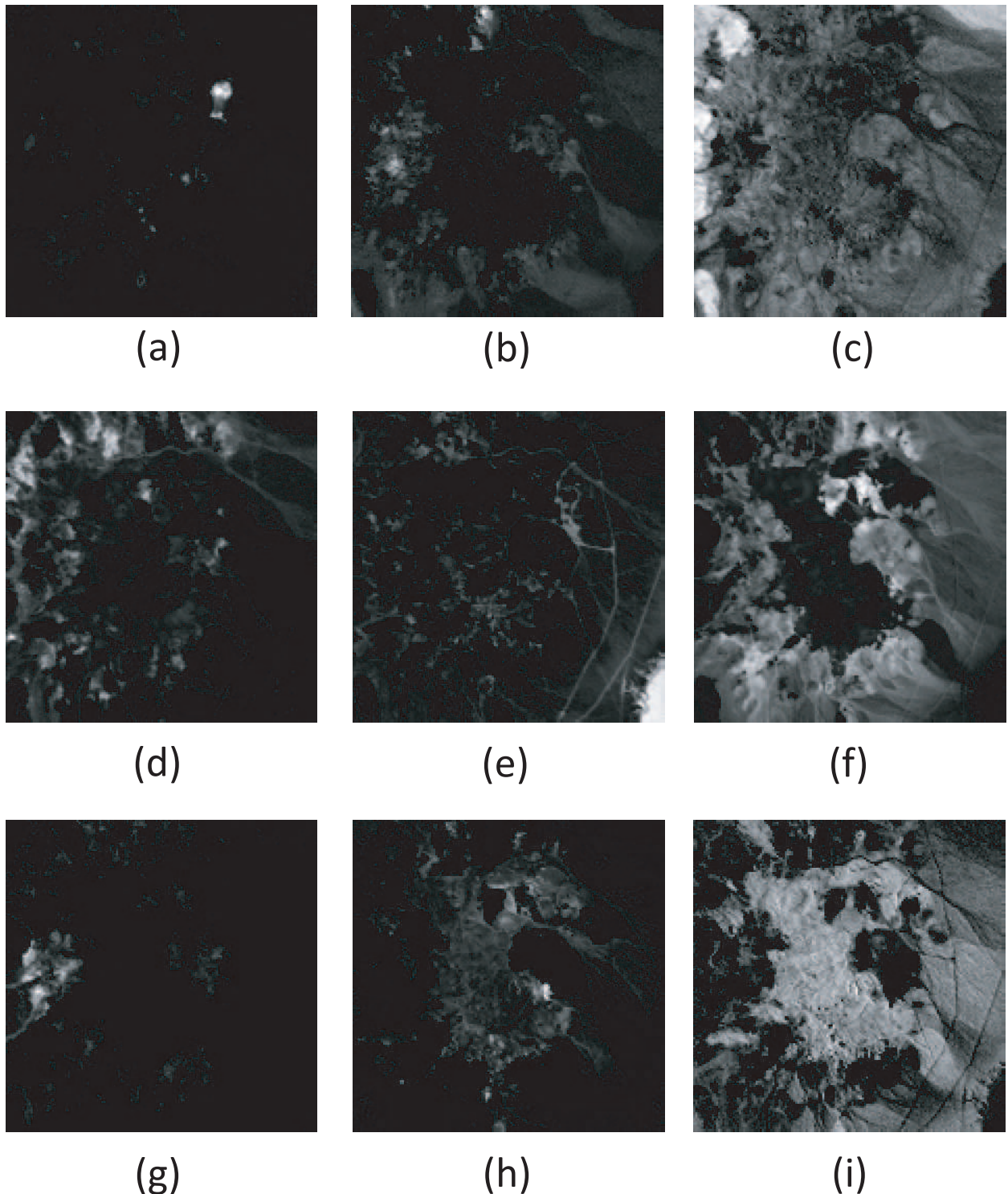


Figure 5. Nine estimated abundance maps by ELMM for Case 1 (without artificial outliers), where (a) Muscovite, (b) Dumortierite, (c) Pyrope, (d) Hematite, (e) Montmorillonite, (f) Alunite, (g) Buddingtonite, (h) Chalcedony, and (i) Andradite, and the gray level scale is between 0 (black) and 1 (white).

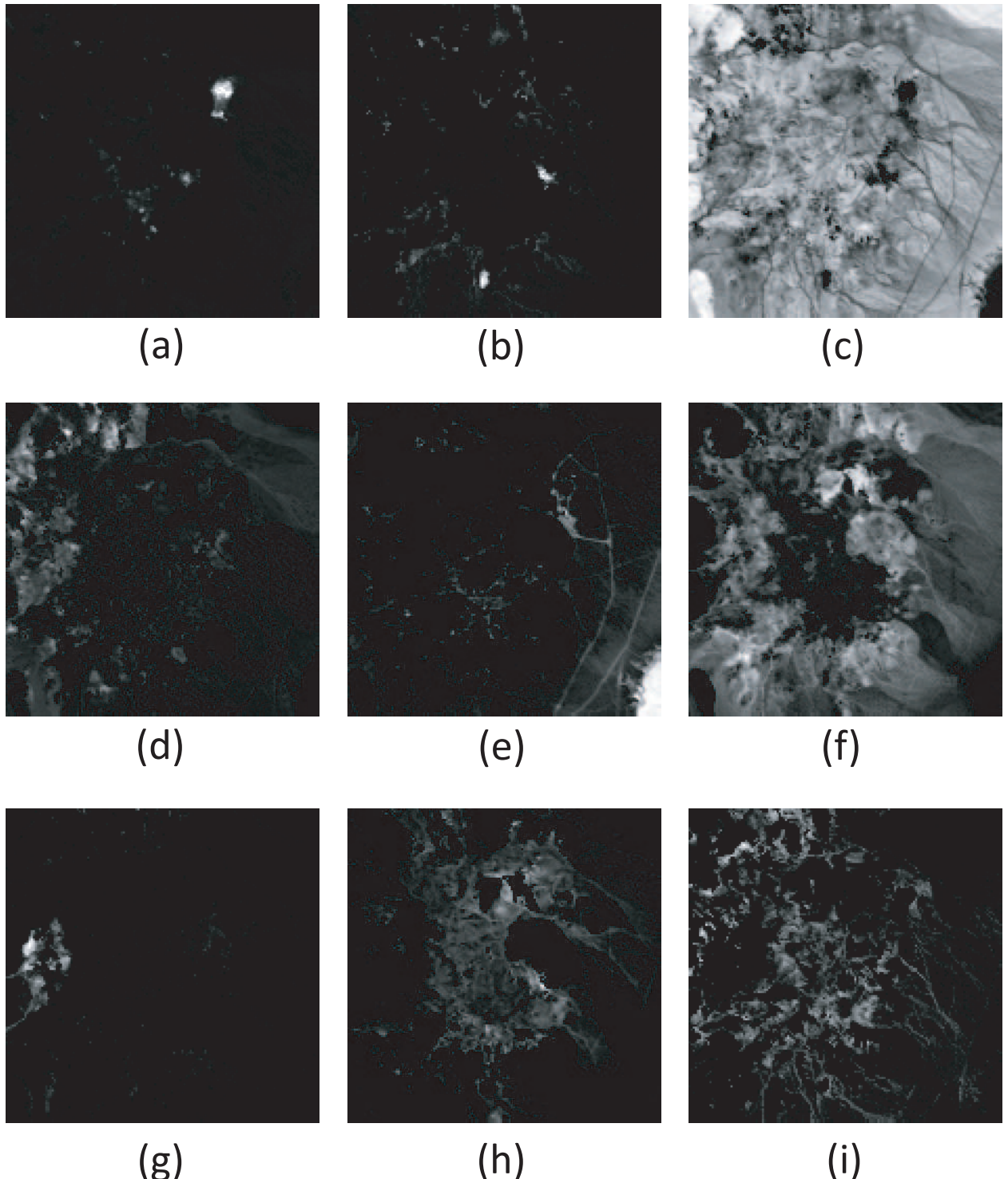


Figure 6. Nine estimated abundance maps by VOIMU for Case 1 (without artificial outliers), where (a) Muscovite, (b) Kaolinite, (c) Pyrope, (d) Hematite, (e) Montmorillonite, (f) Alunite, (g) Buddingtonite, (h) Chalcedony, and (i) Nontronite, and the gray level scale is between 0 (black) and 1 (white).

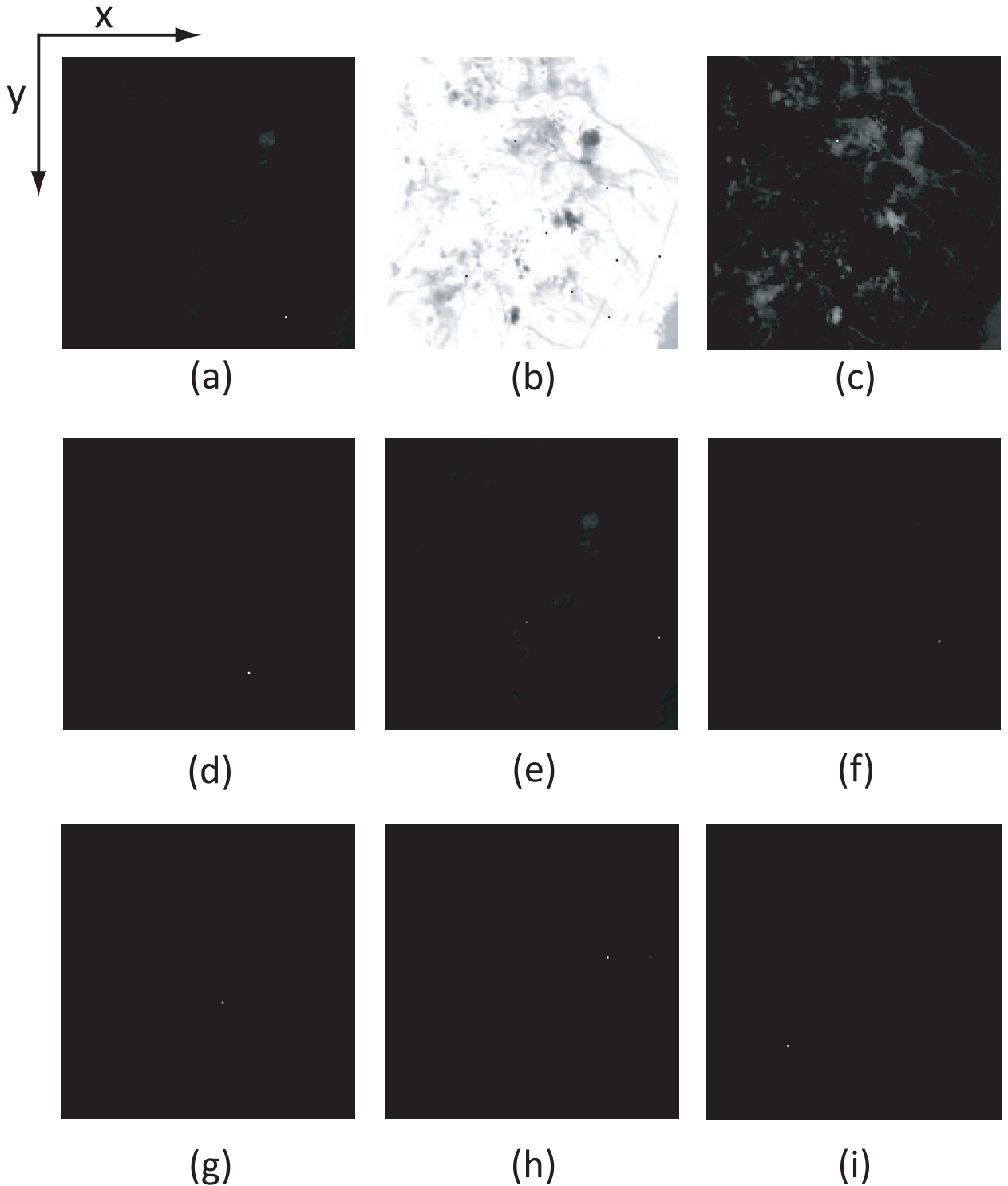


Figure 7. Nine estimated abundance maps by VCA/FCLS for Case 2 (with 10 artificial outliers), where the gray level scale is between 0 (black) and 1 (white).

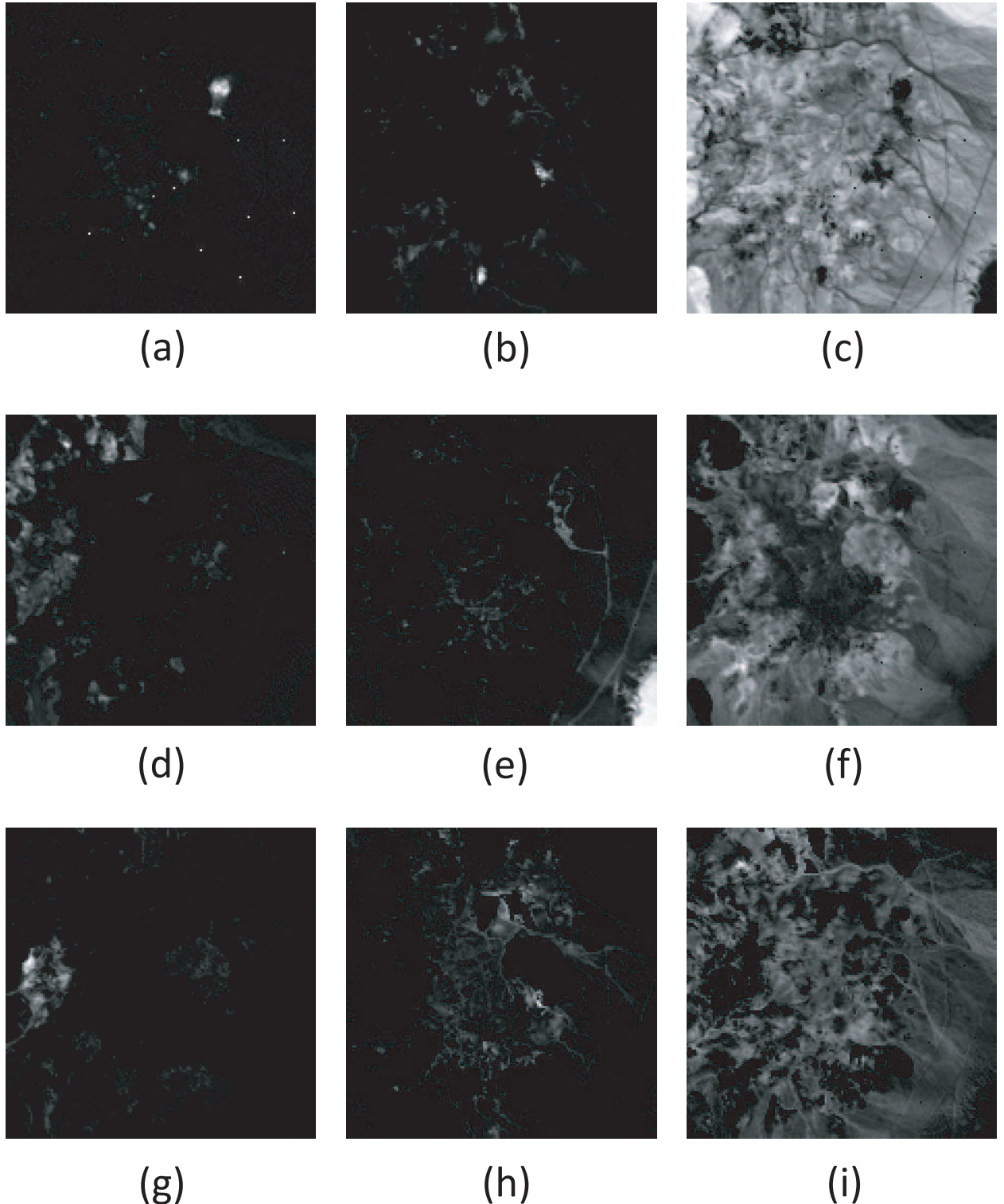
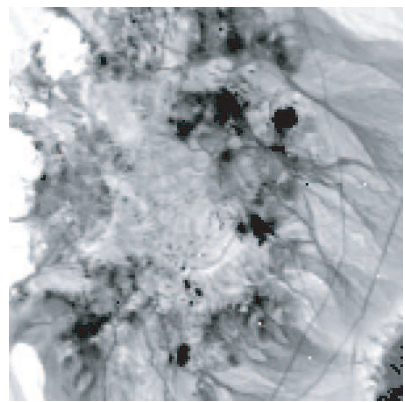


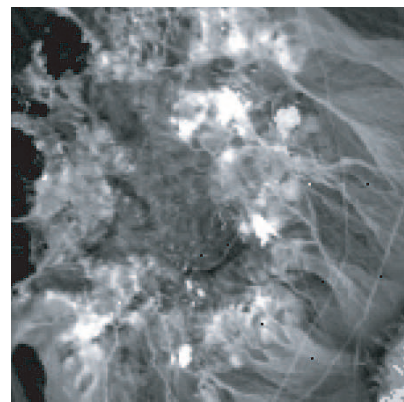
Figure 8. Nine estimated abundance maps by SDVMM-RASF/FCLS for Case 2 (with 10 artificial outliers), where (a) Muscovite, (b) Kaolinite, (c) Pyrope, (d) Hematite, (e) Montmorillonite, (f) Alunite, (g) Buddingtonite, (h) Chalcedony, and (i) Nontronite, and the gray level scale is between 0 (black) and 1 (white).



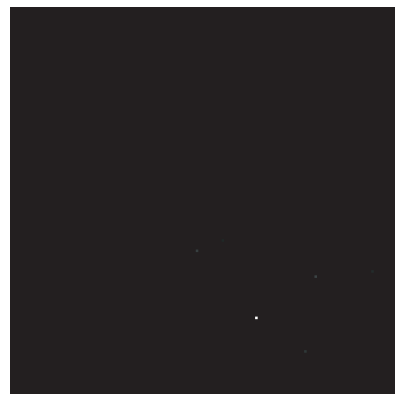
(a)



(b)



(c)



(d)



(e)



(f)



(g)



(h)



(i)

Figure 9. Nine estimated abundance maps by PLMM for Case 2 (with 10 artificial outliers), where the gray level scale is between 0 (black) and 1 (white).

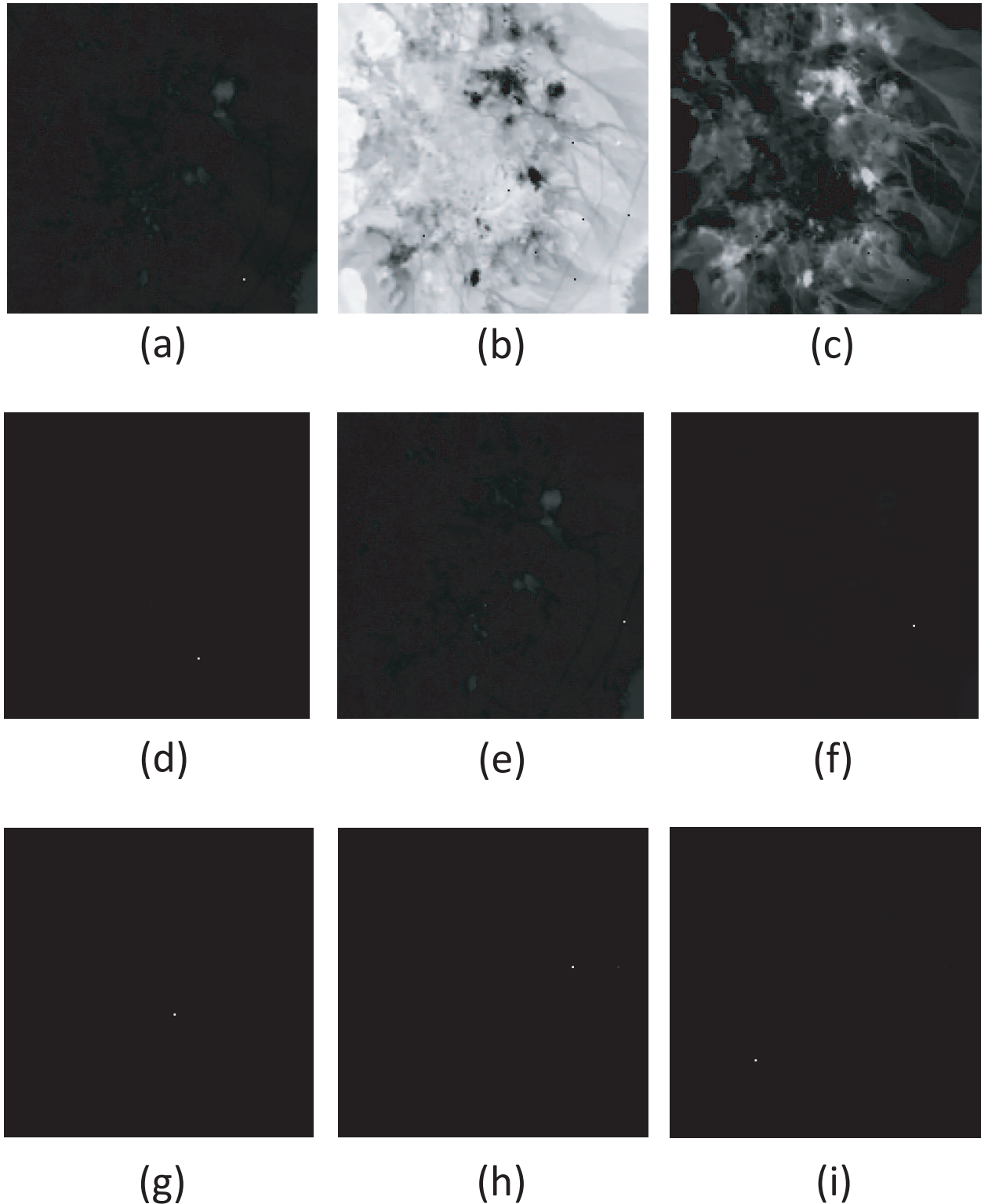


Figure 10. Nine estimated abundance maps by ELMM for Case 2 (with 10 artificial outliers), where the gray level scale is between 0 (black) and 1 (white).

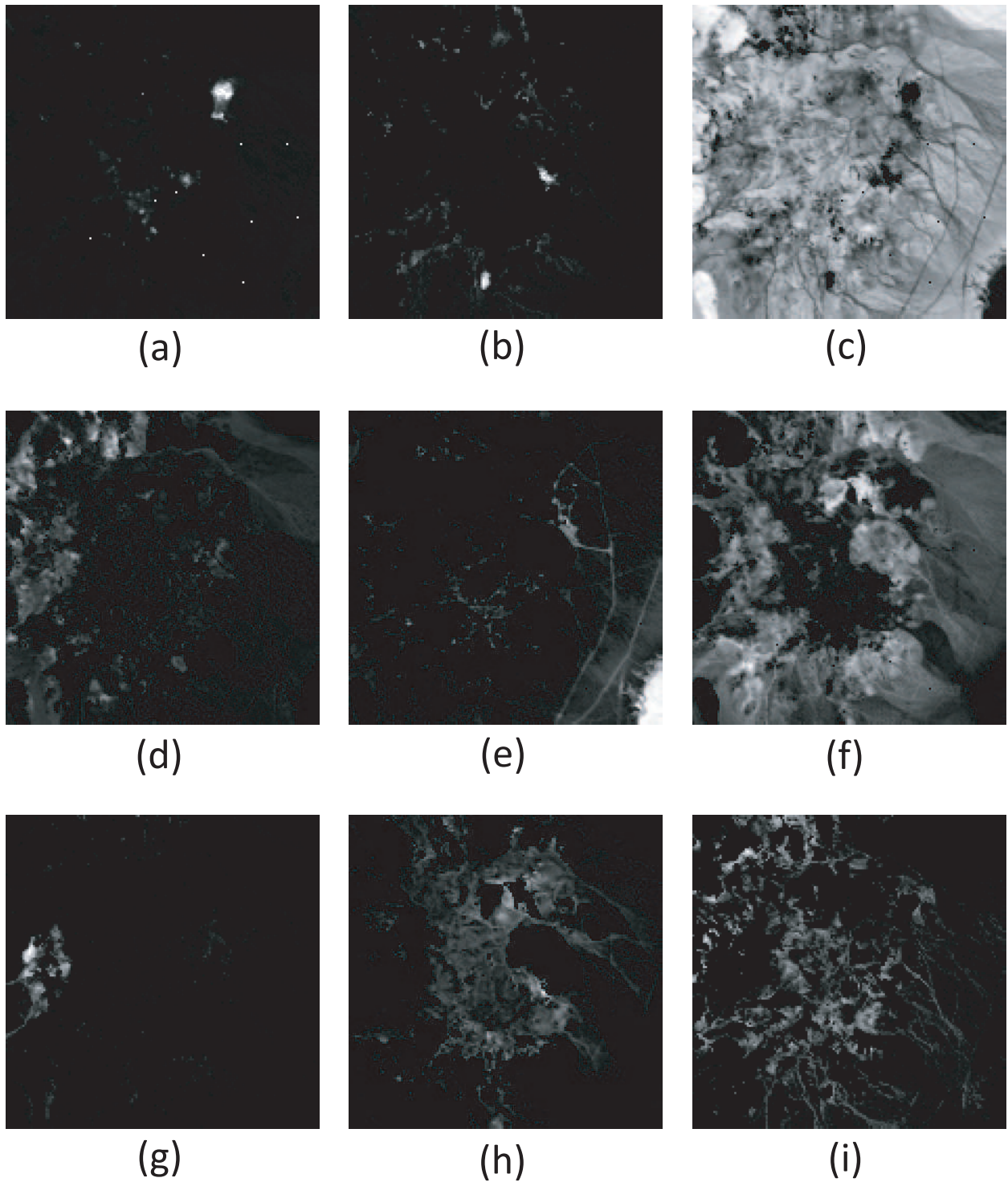


Figure 11. Nine estimated abundance maps by VOIMU for Case 2 (with 10 artificial outliers), where (a) Muscovite, (b) Kaolinite, (c) Pyrope, (d) Hematite, (e) Montmorillonite, (f) Alunite, (g) Buddingtonite, (h) Chalcedony, and (i) Nontronite, and the gray level scale is between 0 (black) and 1 (white).

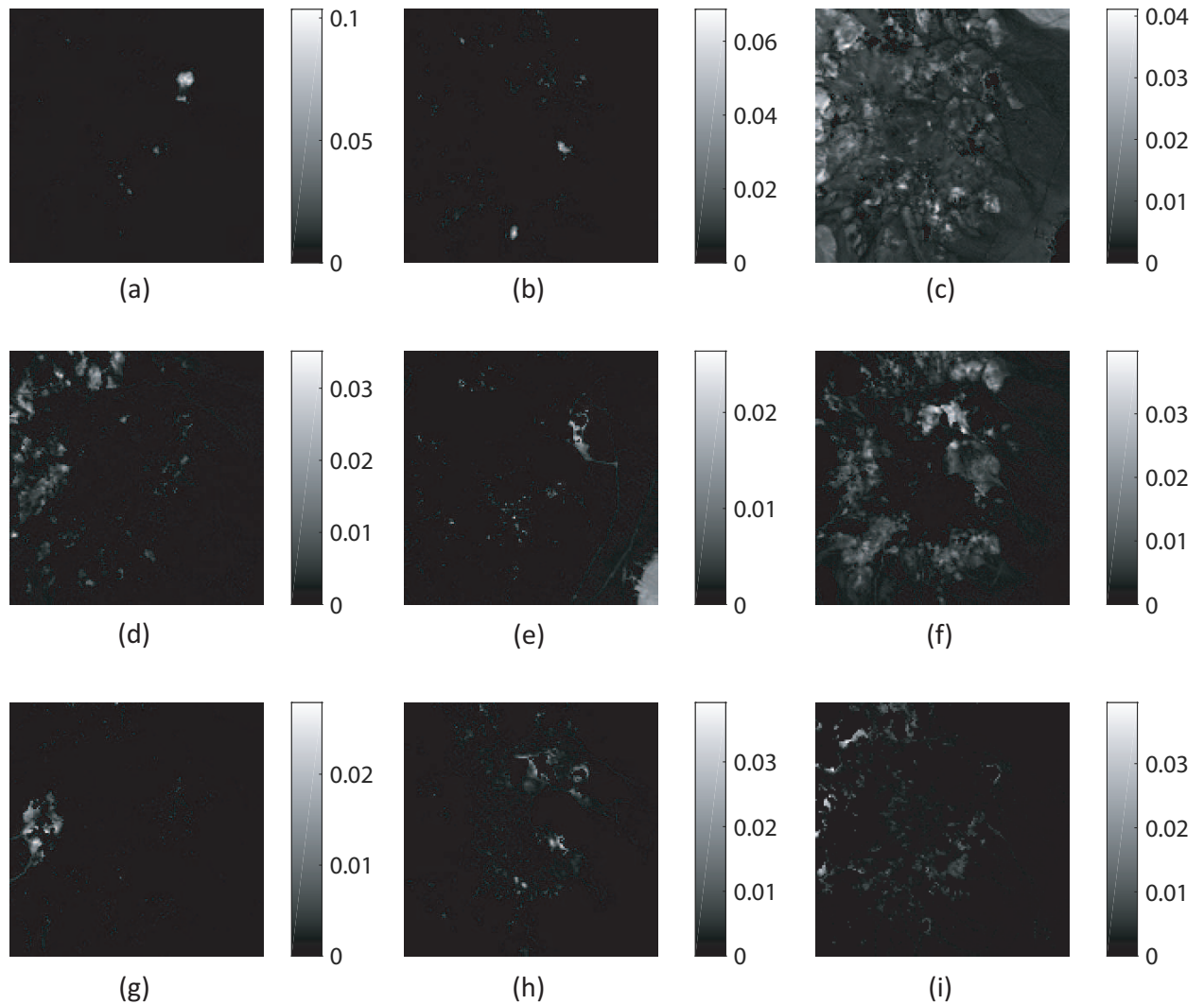


Figure 12. The corresponding square root of EV energy distribution associated with VOIMU for Case 1, where (a) Muscovite, (b) Kaolinite, (c) Pyrope, (d) Hematite, (e) Montmorillonite, (f) Alunite, (g) Buddingtonite, (h) Chalcedony, and (i) Nontronite.

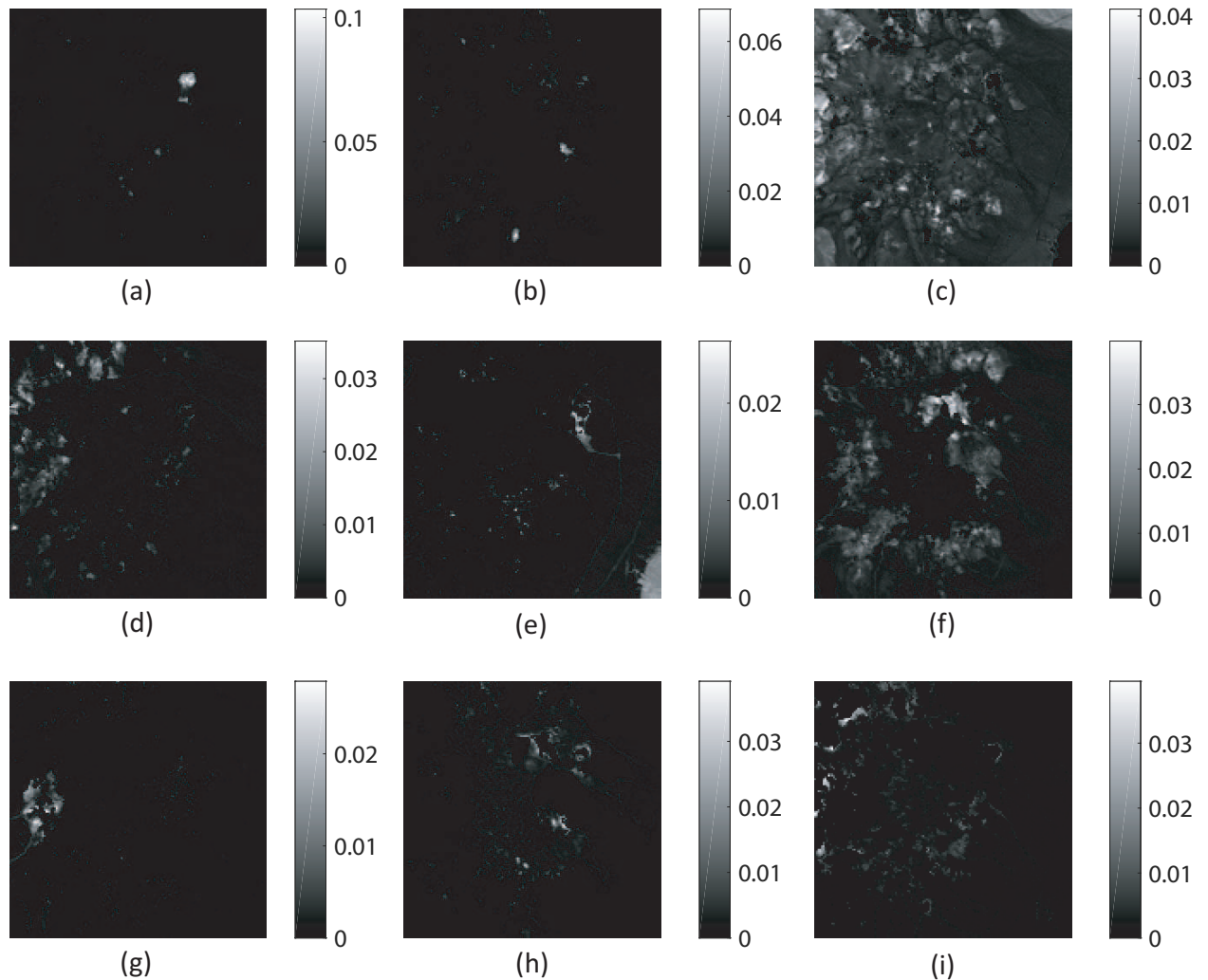


Figure 13. The corresponding square root of EV energy distribution associated with VOIMU for Case 2, where (a) Muscovite, (b) Kaolinite, (c) Pyrope, (d) Hematite, (e) Montmorillonite, (f) Alunite, (g) Buddingtonite, (h) Chalcedony, and (i) Nontronite.

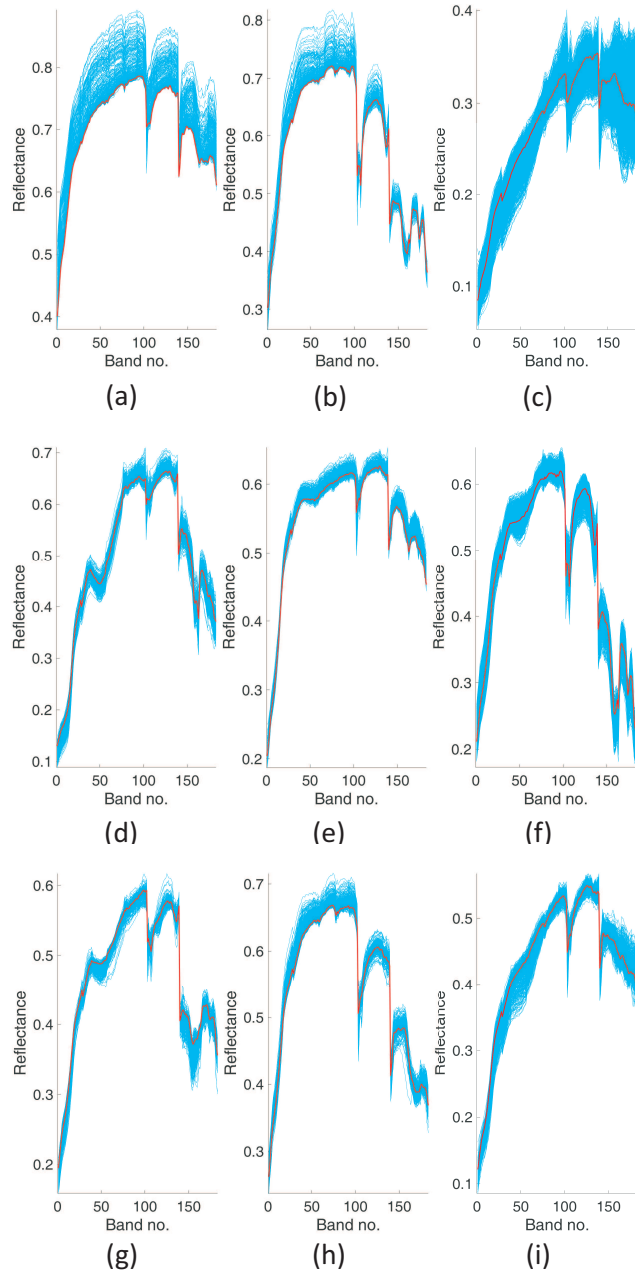


Figure 14. Nine estimated endmember signatures $\hat{\mathbf{A}}_n$ (blue line) and the estimated reference signatures $\bar{\mathbf{A}}$ (red line) by VOIMU for Case 1, where (a) Muscovite, (b) Kaolinite, (c) Pyrope, (d) Hematite, (e) Montmorillonite, (f) Alunite, (g) Buddingtonite, (h) Chalcedony, and (i) Nontronite.

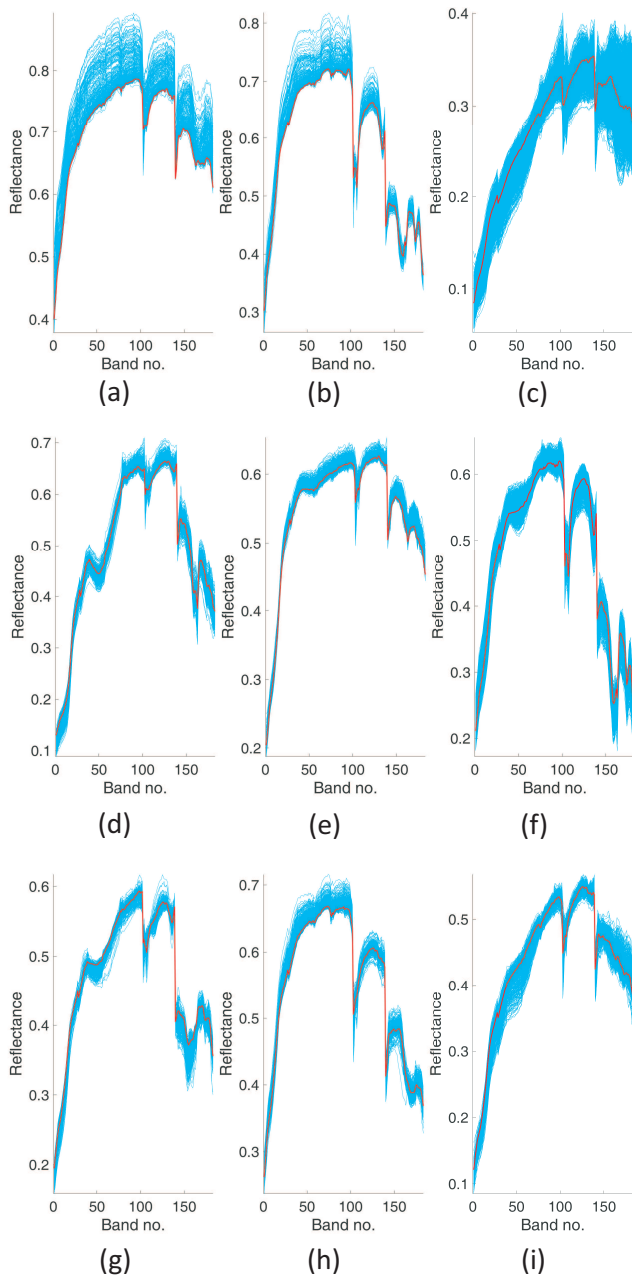


Figure 15. Nine estimated endmember signatures $\hat{\mathbf{A}}_n$ (blue line) and the estimated reference signatures $\bar{\mathbf{A}}$ (red line) by VOIMU for Case 2, where (a) Muscovite, (b) Kaolinite, (c) Pyrope, (d) Hematite, (e) Montmorillonite, (f) Alunite, (g) Buddingtonite, (h) Chalcedony, and (i) Nontronite.

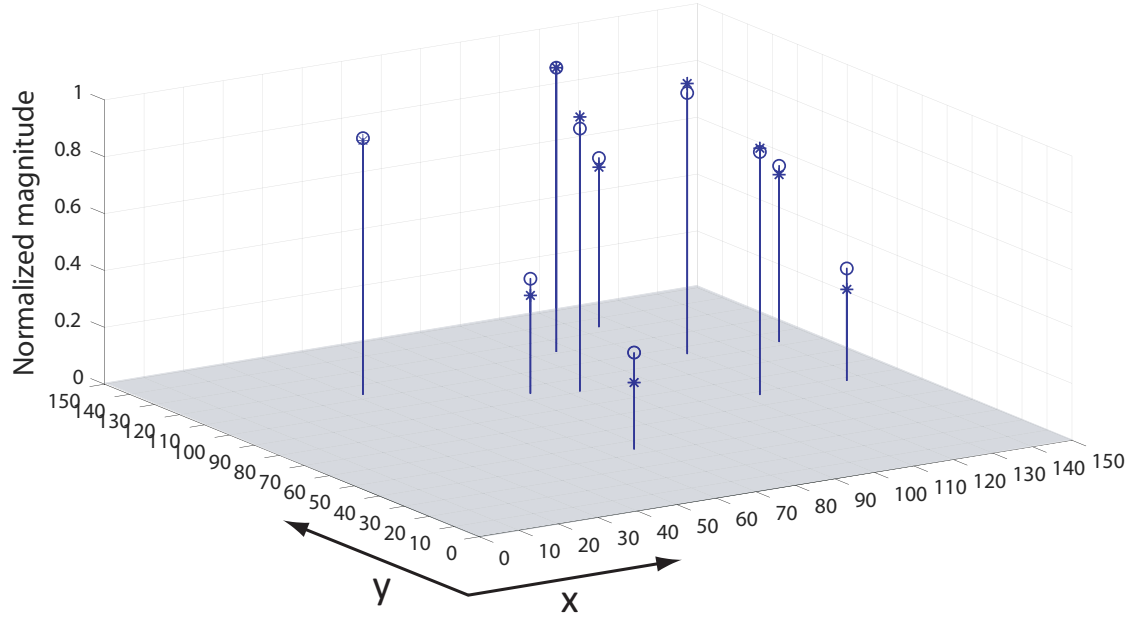


Figure 16. The distribution of the normalized $1/z_n^*$ exceeding a threshold (denoted as circles) for Case 2, where true artificial outliers are denoted as “*”.

References

- [1] Y.-R. Syu, C.-H. Lin, and C.-Y. Chi, “An outlier-insensitive unmixing algorithm with spatially varying hyperspectral signatures,” *accepted for publication as a regular paper in IEEE Access*, 2018.
- [2] C.-I. Chang and Q. Du, “Estimation of number of spectrally distinct signal sources in hyperspectral imagery,” *IEEE Trans. Geosci. Remote Sens.*, vol. 42, no. 3, pp. 608–619, Mar. 2004.
- [3] C.-H. Lin, C.-Y. Chi, Y.-H. Wang, and T.-H. Chan, “A fast hyperplane-based minimum-volume enclosing simplex algorithm for blind hyperspectral unmixing,” *IEEE Trans. Signal Process.*, vol. 64, no. 8, pp. 1946–1961, Apr. 2016.
- [4] P.-A. Thouvenin, N. Dobigeon, and J.-Y. Tourneret, “Hyperspectral unmixing with spectral variability using a perturbed linear mixing model,” *IEEE Trans. Signal Process.*, vol. 64, no. 2, pp. 525–538, Jan. 2016.
- [5] L. Drumetz, M.-A. Veganzones, S. Henrot, R. Phlypo, J. Chanussot, and C. Jutten, “Blind hyperspectral unmixing using an extended linear mixing model to address spectral variability,” *IEEE Trans. Image Process.*, vol. 25, no. 8, pp. 3890–3905, Aug. 2016.
- [6] T.-H. Chan, A. Ambikapathi, W.-K. Ma, and C.-Y. Chi, “Robust affine set fitting and fast simplex volume max-min for hyperspectral endmember extraction,” *IEEE Trans. Geosci. Remote Sens.*, vol. 51, no. 7, pp. 3982–3997, Jul. 2013.
- [7] D. C. Heinz and C.-I. Chang, “Fully constrained least squares linear spectral mixture analysis method for material quantification in hyperspectral imagery,” *IEEE Trans. Geosci. Remote Sens.*, vol. 39, no. 3, pp. 529–545, Mar. 2001.
- [8] J. M. P. Nascimento and J. M. Bioucas-Dias, “Vertex component analysis: A fast algorithm to unmix hyperspectral data,” *IEEE Trans. Geosci. Remote Sens.*, vol. 43, no. 4, pp. 898–910, Apr. 2005.